The 2009 IEEE/RSJ International Conference on
Intelligent Robots and Systems
October 11-15, 2009 St. Louis, USA

Compliant Footpad Design Analysis for a Bio-Inspired Quadruped Amphibious Robot

Hyun Soo Park and Metin Sitti
Department of Mechanical Engineering,
Carnegie Mellon University, Pittsburgh, PA 15213

***Abstract*— A quadrupedal water runner robot inspired by the basilisk lizard has previously demonstrated the capability of water surface locomotion. Since the robot is aimed for the amphibious locomotion, a compatible design on both ground and water surface is discussed in this paper. A compliant footpad which can transfer elastic energy to propulsive momentum is introduced and modeled using a pseudo-rigid-body model. Dynamic modeling of the footpad and the robot provides a criterion of efficient ground locomotion. For the water surface locomotion, drag force can be reduced by compliance of the footpad. The optimized design taking into account two locomotions is studied and analyzed for stability using the Poincaré map.**

I. Introduction

Small animals and insects utilize diverse techniques to float and locomote upon the surface of water. For example, water striders and spiders, which are very light-weight insects and arachnids, use surface tension [1], [2]. Most heavy animals with masses greater than one gram that stay at the air-water interface, such as aquatic birds, rely on buoyancy. Only basilisk lizards and shore birds dominantly use the drag forces exerted by the fast motion of their feet on the water to take advantage of hydrodynamics for locomotion [3].

Biologically inspired robots are those robotic systems which imitate some aspects of living organisms. There is considerable literature about aquatic and amphibious robots that use buoyancy and surface tension [4]–[6]. Yet only the water runner robot employs momentum transfer, similar to a basilisk lizard [7]. A basilisk lizard's ability to locomote on both ground and water using the same legged running mechanism would be a desirable trait for mimicry in robots. Such ability will extend insight into both nature and potential robotics applications. The objective is not to mimic nature, but to understand the principles of operation, and to apply them to accomplish challenging tasks.

The ultimate goal of the water runner is to design the autonomous amphibious robotic systems using the legged mechanisms. Previously, for water surface locomotion, the running frequency required for generating enough lift force was specified as 7-11 Hz where the air cavity is preserved and key design parameters were discussed [8]. Moreover, passive/active tails were proposed and tested to stabilize the pitch motion. Eventually, the robustness of the system for possible disturbances was investigated and experimental models were tested to verify simulations and stability [9]. From these analyses, it was shown that stable water surface locomotion with the legged mechanisms by generating drag could be achieved. However, no compatible design for ground and water locomotion has been studied yet. To resolve these challenging tasks, a compatible design for amphibious locomotion will be discussed and its stability will be analyzed in this paper.

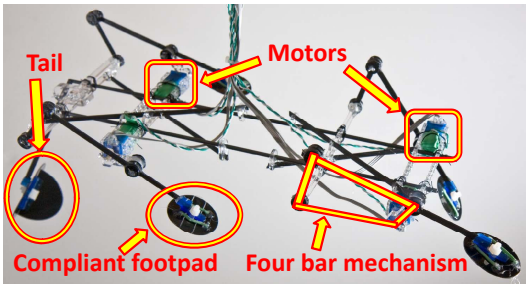

Fig. 1. Photograph of the four-legged water runner robot inspired by basilisk lizards.

II. Robot Description and Animal Locomotion

The water runner [9] has a mass of about 100g, contains four miniature DC motors, and has four legs as shown in Fig. 1. It is 300mm long, 125mm wide, with much of the mass concentrated in the motors, located far from the center of the robot, as shown in Fig. 2. Each leg is driven by one motor, and employs four-bar mechanisms so that the foot trajectory of the robot mimics that of basilisk lizards. Each foot is a circle, 40mm in diameter, with directional compliance which allows it to hit the water while flat, and fold during pullout, reducing undesired drag effects [10].

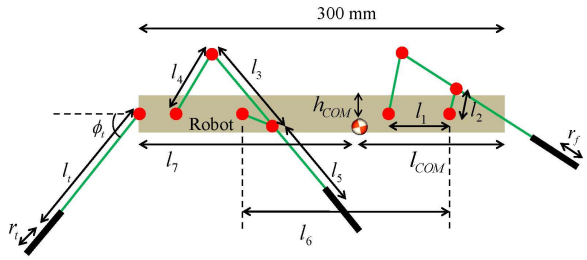

Fig. 2. Geometry and dimensions of the robot: Lengths of the four-bar linkage is presented in TABLE I.

Robot Specification		Link Length	
Robot Length (m)	0.3	l_1 (m)	0.0615
Robot Width (m)	0.125	l_2 (m)	0.0218
Robot Mass (kg)	0.1	l_3 (m)	0.0748
Moment of Inertia		l_4 (m)	0.0468
Roll (kg m^2)	5.05×10^{-4}	l_5 (m)	0.0624
Pitch (kg m^2)	1.08×10^{-3}	l_6 (m)	0.17325
Yaw (kg m^2)	1.24×10^{-3}	l_7 (m)	0.18
Center of Mass (COM) and Footpad		l_t (m)	0.1
l_{COM} (m)	0.12	ϕ_t (°)	30
h_{COM} (m)	0.002	r_t (m)	0.03
r_f (m)	0.02		

TABLE I

ROBOT SPECIFICATIONS AND DIMENSIONS.

For an animal locomotion, the behavior of the center of mass depends on Froude number, $Fr = V^2/gL$, where V is running speed, g is gravitational acceleration, and L is the length from the center of mass to the ground. It is known that if $Fr \approx 0.5$, it shows inverted pendulum style walking. If it is higher than 0.5, then the locomotion can be interpreted as running like the spring-mass model in which kinetic and potential energies are in phase [11]–[13]. For the spring-mass model, an animal utilizes elastic energy stored in the leg muscles to propel the center of mass. Since Fr of an adult basilisk lizard is mostly higher than 2, when it approaches the water surface, the spring-mass model is matched to ground locomotion of the water runner.

Due to the fact that the weight of the robot is critical, a spring-like active leg may be inappropriate because adding actuators can increase its mass significantly. Rather than actuation, a passive compliant footpad attached at the end of the leg which can reduce design complexity and the number of additional parts is more suitable and is studied in this paper. For roll and pitch stability of the ground locomotion, the robot is assumed to have a trot gait in which diagonal pairs are in phase and a passive tail which stabilizes pitch motion so that only vertical and horizontal motions of the robot are discussed. Furthermore, as the controller of the experimental model of the water runner is used to generate constant angular velocity at an input link of the four-bar, an input link in simulation is also assumed to rotate at a constant running frequency.

In addition, the robot is aimed to be autonomous for transient locomotion. Some existing amphibious robotic systems [14] use a remote control to change behaviors for different environments. Nevertheless, we will explore generic dynamics which can be compatible for both environments without changing modes manually. Thus, even though the running speed on ground does not need to be as high as that on the water's surface, around 7-11 Hz, all running frequencies, ω_{ru}, up to 7 Hz, which is the minimum frequency for transition will be tested for stable ground locomotion.

III. Compliant Footpad Design Optimization

A. Ground Locomotion Modeling

For large deflection of a beam, since the Bernoulli-Euler beam equation becomes nonlinear, force-deflection relations cannot be solved by simple secondary ordinary differential equations. Meanwhile, understanding behaviors of a compliant member are crucial to analyze ground locomotion dynamics because a compliant member attached at a footpad deflects highly for given external forces. Instead of solving the Bernoulli-Euler beam equation, kinematic and dynamic analyses of a compliant mechanism have been studied by introducing the pseudo-rigid-body model (PRBM) which simplifies to a mechanism composed of rigid body links and torsional springs [15]–[17]. The PRBM provides effective tools to analyze the deflection trajectory and elastic energy of the compliant mechanism and is known to be highly accurate. More details about the PRBM can be found in [18].

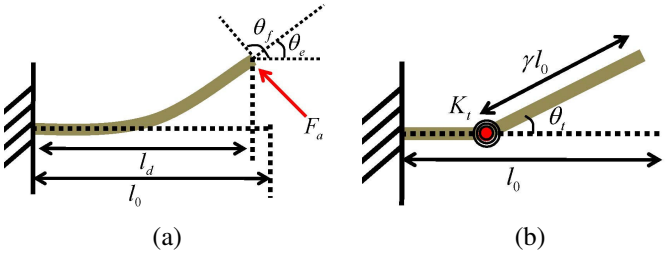

Fig. 3. (a) Deflection of a compliant member (b) The pseudo-rigid-body model using rigid links and a torsional spring.

By curve fitting the trajectory of a deflected beam end, the characteristic radius factor, γ, where a torsional spring is located can be found in terms of the angle, θ_f, in the direction of applied force, as shown in Fig. 3. The stiffness of the compliant member, which linearly relates with the torsional spring constant, can also be approximated by fitting the force-deflection curve in terms of θ_f:

$$\gamma = \gamma(\theta_f) \tag{1}$$

$$K_c = K_c(\theta_f) \tag{2}$$

$$K_t = \gamma K_c \frac{EI}{l_0} \tag{3}$$

where E is Young's modulus, I is cross-sectional area moment of inertia of the beam, and l_0 is the beam's original length. In addition, the beam end angular deflection, θ_e, can be approximated as a function of the angular deflection of the torsional spring, θ_t.

$$\theta_e = \theta_e(\theta_t) \approx c_e(\theta_t)\theta_t \tag{4}$$

where c_e is the parametric angle coefficient found in [15]. Rotational motion of the input link of the four-bar mechanism of water runner's leg generates the footpad trajectory and orientation shown in Fig. 4. As mentioned before, assuming the input link, l_2, rotates with a constant angular velocity, the footpad trajectory, its orientation, and their time derivatives can be attained by mathematical formulation [19]. When the footpad touches down on the ground, external forces such as the ground reaction force make the compliant members deflect so that kinetic and potential energies are converted to elastic energy which would be used for accelerating the center of mass of the robot as shown in Fig. 5. The moment, τ_j, applied at each revolute joint where the torsional

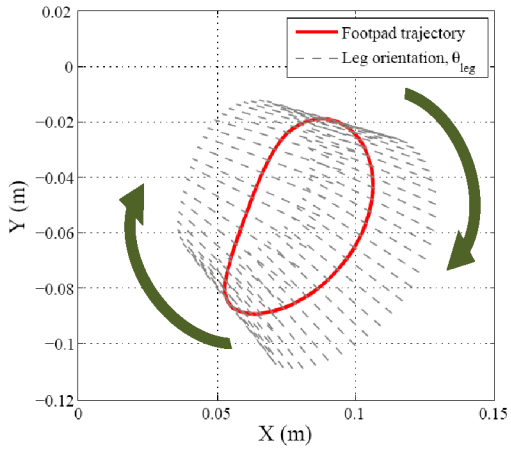

Fig. 4. Simulated trajectory of the foot with footpad orientation shown.

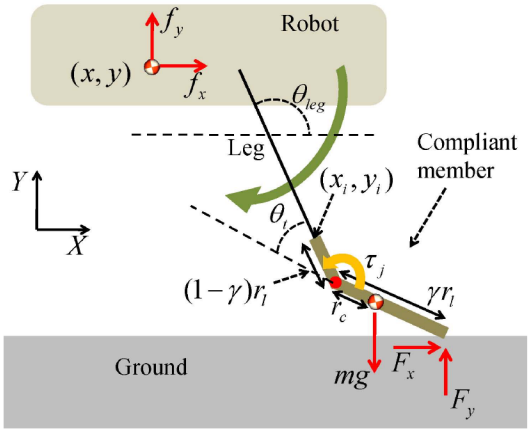

Fig. 5. Geometry of the footpad when it contacts with the ground.

spring is located and the net force, f_x and f_y, exerted at the center of mass of the robot can be obtained by

$$\tau_j = K_t\theta_t - K_d\dot{\theta}_t - \gamma m g r_c \cos(\pi - \theta_{leg} - \theta_t) + \gamma F_y r_l \cos(\pi - \theta_{leg} - \theta_t) + \gamma F_x r_l \sin(\pi - \theta_{leg} - \theta_t) \quad (5)$$

$$f_x = F_x \quad (6)$$

$$f_y = -(0.25m_r + \gamma m)g + F_y \quad (7)$$

where K_d is the damping coefficient chosen carefully to reflect the behavior of the actual compliant member, m is mass of the footpad, m_r is mass of the robot, F_x is the friction force, F_y is the ground reaction force, r_l is the length of the footpad, r_c is the length from the joint to the center of mass of the footpad, and θ_{leg} is the leg orientation.

Although the ground reaction force which takes into account unilateral contact dynamics and the instantaneous impact force is hard to estimate accurately, if contact geometry and kinematics are well defined, it can be approximated by assuming the ground as a visco-elastic element following [20]

$$F_y = \begin{cases} 0.25 \times 10^9 |y_p|^3 (1 - \dot{y}_p) & \text{if } y_p > 0 \\ 0 & \text{if } y_p \le 0 \end{cases} \quad (8)$$

where y_p and $\dot{y}_p$ are the penetration depth of the contact point and its time derivative, respectively. Since we can always derive position and velocity of the contact point by the geometry, F_y can be specified whenever it penetrates into the ground, i.e. $y_p > 0$.

The friction force, F_x can be due to either static or kinetic friction depending on the magnitude of F_y. When the static friction force is applied, the motion is determined by kinematics of the joint because the footpad is stuck at the contact point and the center of mass of the robot moves relative to the contact point. Otherwise, the footpad slips over the ground. When the time derivative of the propulsive momentum is higher than the static friction force, $\mu_s F_y$, where μ_s is the static friction coefficient, slip occurs. From these conditions, the friction force can be described as

$$F_x = \begin{cases} 0 & \text{if } F_y = 0 \\ (0.25m_r + \gamma m)a_x & \text{if } (0.25m_r + \gamma m)a_x < \mu_s F_y \\ \mu_k F_y & \text{if } (0.25m_r + \gamma m)a_x \ge \mu_s F_y \end{cases} \quad (9)$$

$$\begin{aligned} a_x &= \frac{\mathrm{d}^2}{\mathrm{d}t^2}\left[-x_i + (1-\gamma)r_l \cos\theta_{leg} + \gamma r_l \cos(\theta_{leg} + \theta_t)\right] \\ &= -\ddot{x}_i - (1-\gamma)r_l(\ddot{\theta}_{leg}\sin\theta_{leg} + \dot{\theta}_{leg}^2 \cos\theta_{leg}) \\ &\quad - \gamma r_l[(\ddot{\theta}_{leg} + \ddot{\theta}_t)\sin(\theta_{leg} + \theta_t) + (\dot{\theta}_{leg} + \dot{\theta}_t)^2 \cos(\theta_{leg} + \theta_t)] \end{aligned} \quad (10)$$

where μ_k is the kinetic friction coefficient, a_x is the second derivative of the position of the center of mass of the robot when the static friction force is applied, and x_i is the joining point between the compliant member and the leg.

The equations of motion of each joint and the center of mass of the robot can be formulated as

$$\ddot{\theta}_t = M_j/(\mathcal{I} + \gamma m r_c^2) \quad (11)$$

$$\ddot{x} = f_x/(0.25m_r + \gamma m) \quad (12)$$

$$\ddot{y} = f_y/(0.25m_r + \gamma m) \quad (13)$$

where $\mathcal{I}$ is the moment of inertia of the footpad and x, y are position of the center of mass of the robot. Since $\ddot{x}$, $\ddot{y}$ of (12), (13) are accelerations for only one footpad, each equation of motion of each footpad should be superposed to account four legs.

Figure 6 shows how the joint angle, θ_t, deflects with respect to leg orientation, θ_{leg}, when $EI = 7.65 \times 10^{-4}$Pa m^4 and $\omega_{ru} = 3$ Hz. Deflection of the joint angle starts when the tip of the footpad touches down on the ground and then it shows spring-damper behavior when it takes off. From (4), the end deflection angle, θ_e, of the compliant member can be obtained and the contact angle, $\theta_{ct} = \pi - \theta_{leg} - \theta_e$, which is the orientation of the tip of the compliant member is plotted in Fig. 7. When θ_{ct} becomes less than 0, surface contact starts so that it helps to transfer the friction force to forward momentum effectively due to stable contact. Also, it enhances locomotion stability because it increases the area of the supporting polygon, which the center of the mass of the robot should be located inside.

Figure 8 shows how the center of mass of the robot behaves. Vertical motion is synchronized with the legs' motion which rotate with running frequency, ω_{ru}, so that

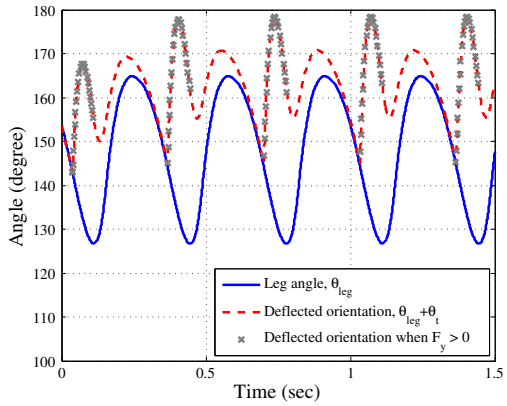

Fig. 6. When the footpad touches down the ground, the deflection of the compliant member starts due to the ground reaction force and when taking off, it behaves like the spring-damper systems i.e. $\theta_t \to 0$.

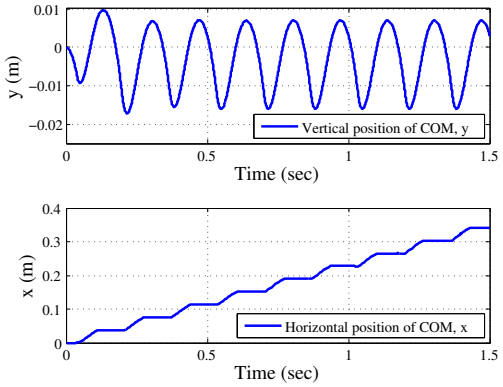

Fig. 8. Position of the center of mass of the robot, x, y, are plotted for $EI = 7.65 \times 10^{-4}$Pa m^4 and $\omega_{ru} = 3$ Hz. Vertical motion gets synchronized with $2\omega_{ru}$ (trot gait) at 0.3 second. Alternating acceleration and deceleration of horizontal motion results that the robot can travel forward steadily.

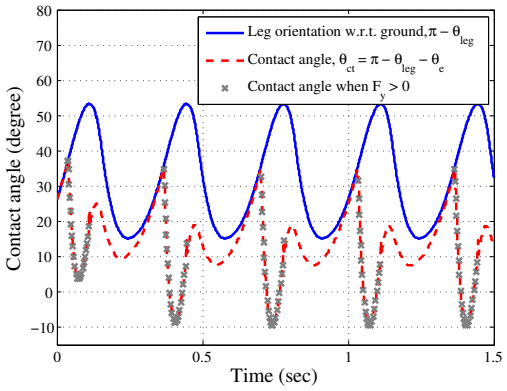

Fig. 7. Contact angle, θ_{ct}, of the compliant member shows how the footpad is stably contact with ground. When surface contact occurs, $\theta_{ct} < 0$, locomotion stability can be enhanced.

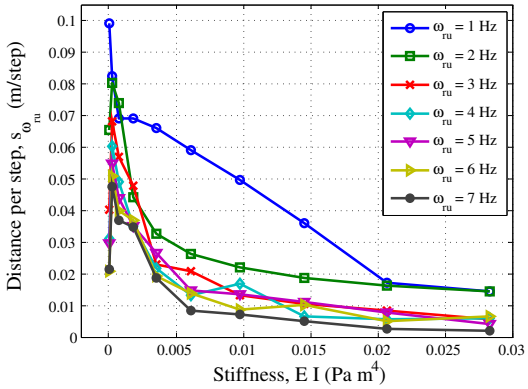

Fig. 9. Elastic energy stored in the compliant member is used to propel the center of mass of the robot forward. Small stiffness transfers propulsive momentum more effectively due to stable contact which increases contact time for a given step. Thus, distance per step can show how effectively the robot travels forward.

it enters steady state in 0.3 seconds. For lateral motion, the friction force induces acceleration and deceleration alternatingly; when contact is started, the stepping ground accelerates the center of mass and when the footpad takes off, it decelerates. For the spring-mass model, elastic energy stored in the spring with various stiffness is constant due to energy conservation law in the vertical direction; when the spring is fully displaced, the total energy, which is the sum of kinetic and potential energies, is converted to elastic energy. However, propulsive momentum transfer is different depending on the stiffness. For high stiffness, large EI, it is low because of bouncing behavior of the contact point. Since a small displacement of the compliant member generates excessive ground reaction force, the contact point does not stay on the ground but bounces whenever it touches down, which causes insufficient contact time to accelerate the center of mass of the robot. Thus, the robot cannot propel effectively for a given step. Figure 9 shows how much the robot travels per each step, $s_{\omega_{ru}}$, depending on the stiffness of the compliant member. The higher the stiffness, the less distance traveled per step. For too low stiffness, $EI = 2.83 \times 10^{-5}$Pa m^4, contact time of each footpad is so long that contact time of both sides is overlapped (double supporting phase), which causes reduction of acceleration by the opposing directions of friction forces.

B. Water Surface Locomotion

As far as the locomotion on the water surface is concerned, the compliance of a footpad can reduce the lift force because the drag force proportional to water contact area can be reduced due to deflection by hydrodynamic pressure. Since water contact area is proportional to the projected length of deflected compliant member, l_d, onto original length, l_0, as shown in Fig. 3(a), the ratio l_d/l_0 is directly proportional to total lift force. Solving with the finite element program, ANSYS, deflection of the compliant member with uniformly distributed hydrodynamic pressure is tested. Hydrodynamic pressure for a given running frequency can be obtained by integrating the drag, D, through infinitesimal areas divided by total water contact area, A, as follows [8]

$$D = \frac{C_D^* \int_A (0.5\rho u^2 + \rho g h) \mathrm{d}A}{A} \tag{14}$$

where $C_D^* = 0.707$ is the drag coefficient for a flat, circular disk in presence of air cavity, ρ is the density of the water, u is the normal velocity of the footpad, h is depth of the foot below the water's surface. Since the maximum deflection occurs at the maximum drag, loading pressure on the beam is chosen as the highest drag during one rotation cycle.

For boundary conditions in the analysis, the left end of a 40 mm long beam is constrained in all degrees of freedom with a free right end. Then uniformly distributed load obtained from (14) is applied along the beam. Various hydrodynamic pressures corresponding to running frequency of 7-11 Hz are tested for different stiffnesses of the beam. Since $(1\text{-}l_d/l_0)$ is proportional to the reduction of the lift force, which needs to be minimized, the less reduction, the more desirable lift force for a given running frequency, as shown in Fig. 10. When testing with lower than $EI < 2.27 \times 10^{-4}$Pa m^4, the reduction is set to be 100% because too much deflection results in higher than 100% reduction which is unrealistic. As expected, higher stiffness results in a smaller percentage of the reduction of the lift force, which is desirable.

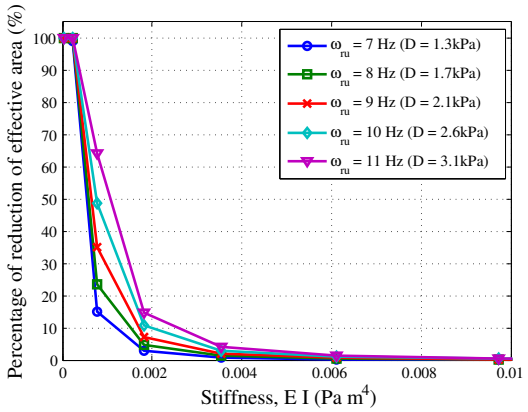

Fig. 10. The compliant member attached at the end of the leg deflects when running in water because of hydrodynamic pressure, D. Percentage of the reduction of water contact area, $100(1 - l_d/l_0)$, can provide the lift force reduction. Stiffness higher than 0.006Pa m^4 shows almost 0% reduction.

C. Optimization

While low stiffness shows efficient and stable ground locomotion, it causes high reduction of the lift force for the water interaction. Thus, the stiffness of the compliant member should be optimized to be compatible for both environments. On the one hand, distance per step, $s_{\omega_{ru}}$, normalized by $s_{max} = \texttt{max}\{s_{\omega_{ru}}\}$ can represent the performance of the ground locomotion. On the other hand, the ratio l_d/l_0 can be water locomotion performance. From these, the cost function, Ψ, can be defined as the following and the stiffness of the compliant member can be selected by minimizing this cost.

$$\Psi = \frac{1}{w_w + w_g}\left[w_w \sum_{\omega_{ru}=7\text{Hz}}^{11\text{Hz}} \left(1 - \frac{l_{d,\omega_{ru}}}{l_0}\right)^2 + w_g \sum_{\omega_{ru}=1\text{Hz}}^{7\text{Hz}} \left(1 - \frac{s_{\omega_{ru}}}{s_{max}}\right)^2\right] \tag{15}$$

w_w and w_g are the weights for each locomotion, which controls their relative importance.

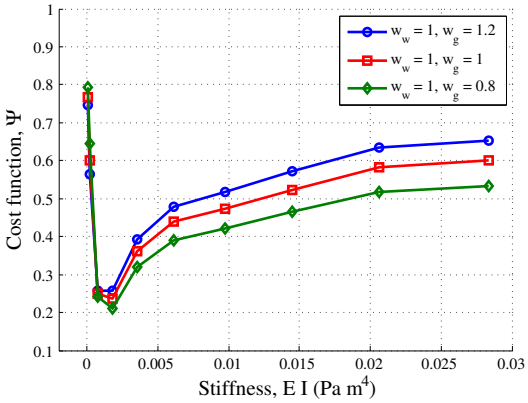

Fig. 11. In order for the compatible design of the footpad, one can choose its stiffness which minimizes the cost function, Ψ, taking into account distance per step and reduction of the lift force. Relative important can be controlled by the weight, i.e. when each locomotion is equally significant, $w_w = 1, w_g = 1$ and when water locomotion is more important, $w_w = 1, w_g = 1$.

The cost function, Ψ, is minimized at $EI = 7.65 \times 10^{-4} \sim 1.81 \times 10^{-3}$Pa m^4 regardless of the choice of weights, as shown in Fig. 11. Therefore, one can choose this range of the stiffness of the footpad for amphibious locomotion.

IV. Stability Analysis

From the optimization, one can select the stiffness but it cannot be said the optimized design is stable through the amphibious locomotion. For the water surface locomotion, we had investigated marginal lift force both in simulations and experiments [9], which shows reduced lift force can still support its weight. Furthermore, roll and pitch motions become more stable if lift force is reduced because external forces disturbing the system are reduced. However, stability on the ground has not been studied for the optimized stiffness of the footpad. Therefore, we will explore the stability of the ground locomotion within the optimized stiffness where 7.65×10^{-4}Pa m^4 $\leq EI \leq 1.81 \times 10^{-3}$Pa m^4 and find a stable regime for the system.

A. Poincaré Map and Floquet Multiplier

Since the system shows nonlinear oscillatory behavior, finding an analytic solution, which is essential to stability analysis, is hard to achieve. Contact forces are nonlinear and oscillatory leg rotation disturbs the system with running frequency. However, a numerical solution from dynamic modeling can provide a trend of the system's behavior. Based on numerical data, we will quantify the stability of the system and find the desirable motion for the amphibious locomotion.

Let us define a state variable, $X = [y\ \dot{y}\ y_i\ \dot{y}_i\ \theta_t\ \dot{\theta}_t]^{\mathrm{T}}$. y shows how the robot's vertical motion behaves and y_i shows how y is synchronized with running frequency. If there is a time dependent function, Φ, such that

$$\Phi(X, t_0)|_t = \Phi(X, t_0)|_{t+T} \tag{16}$$

for some minimum period $T > 0$, then this becomes a limit cycle in state space. If there exists a limit cycle that attracts all nearby trajectories for a given initial state, the system can be said asymptotically stable in Lyapunov sense.

For the 6th-order non-autonomous periodic system, the dynamics can be converted to the 7th-order autonomous system by extending a phase state, $\Theta \in [0\ 2\pi)$, as following [21]

$$\Theta := \mathtt{mod}(2\pi t/T, 2\pi) \tag{17}$$

where mod is the function that restricts to $[0\ 2\pi)$. To be stable, the phase portrait of X for every period, T, which is when $\Theta = \Theta_0$, should show limiting behavior as $t \to \infty$ where Θ_0 is a certain phase in $[0\ 2\pi)$. Define a 6-dimensional hyperplane, σ, a so called Poincaré section, with $\sigma := \{(X, \Theta)|\Theta = \Theta_0\}$ and let P be the map between discretized time sequence of trajectory which intersects the Poincaré section i.e.

$$\begin{aligned} &P : \sigma \to \sigma, \quad X_i \in \sigma \\ &X_{i+1} = P(X_i) \end{aligned} \tag{18}$$

where X_i is the state of the ith intersection of the Poincaré section. P is called the Poincaré map. For a certain state such that $X_f = P(X_f)$, X_f is called the fixed point. Then, the trajectory of the system is asymptotically stable if and only if the fixed point, X_f, is asymptotically stable [22].

By linearizing the Poincaré map in vicinity of X_f, a 6×6 Jacobian matrix, J, maps

$$\Delta X_{i+1} = J(X_f)\Delta X_i \tag{19}$$

where $\Delta X_i = X_i - X_f$. The eigenvalues of J, called the Floquet multipliers, determine discretized system dynamics. If the largest magnitude of the Floquet multiplier is bigger than 1, the system is unstable because any small perturbation yields higher sequential displacement from X_f. If it is strictly smaller than 1, X_f can be said to be asymptotically stable. Thus, if one can find J, it is possible to quantify stability of the system by the magnitude of the Floquet multipliers.

From numerical data, we can construct Y_1 and Y_2 matrices and derive the relation between them [23], [24]:

$$Y_1 = \begin{bmatrix} X_1 & X_2 & \cdots & X_n \end{bmatrix}^{\mathrm{T}} \tag{20}$$

$$Y_2 = \begin{bmatrix} X_2 & X_3 & \cdots & X_{n+1} \end{bmatrix}^{\mathrm{T}} \tag{21}$$

$$\begin{aligned} Y_2 &= Y_1 J^{\mathrm{T}} + B \\ &= [Y_1 1_{n\times 1}] \begin{bmatrix} J^{\mathrm{T}} \\ B \end{bmatrix} \end{aligned} \tag{22}$$

where $B = X_f^{\mathrm{T}}(I - J)^{\mathrm{T}}$, and $1_{n\times 1}$ is an n-dimensional vector where all elements are 1. From the linear least square algorithm,

$$\begin{bmatrix} J^{\mathrm{T}} \\ B \end{bmatrix} = (K^{\mathrm{T}}K)^{-1}K^{\mathrm{T}}Y_2 \tag{23}$$

$$\lambda = \mathtt{eig}(J) \tag{24}$$

where $K = [Y_1 1_{n\times 1}]$, J can be solved and the Floquet multiplier, λ can be obtained.

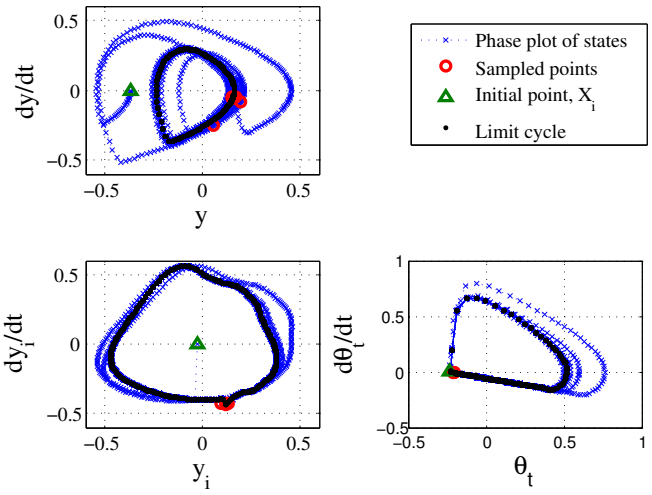

Fig. 12. 2-dimensional phase plots of a state, X, are illustrated for $EI = 1.22 \times 10^{-3}$Pa m^4, ω_{ru} = 5 Hz, and K_d = 0.003Nm s. Each state shows limiting behavior and converges to the limit cycle after a few initial transient cycles, which all Floquet multipliers stay inside of unitary circle in complex plane (λ = −0.2286, 0.003, 0.1782, 0.4910, 0.0792 ± 0.3017i). Therefore, this system converges to limit cycle asymptotically in finite time.

B. Stable Locomotion Regime

Figure 12 illustrates the phase plot and Floquet multipliers for $EI = 1.22\times10^{-3}$Pa m^4, ω_{ru} = 5Hz, and K_d = 0.003Nm s. Each state converges to the limit cycle and sampled points show asymptotic behavior approaching to the fixed point. The settling time when percentage error, $\Delta X_i/\mathtt{max}\{\Delta X_i\}$, becomes less than 2% is 0.8 second. All Floquet multipliers stay in a unitary circle in the complex plane so that this system can be said asymptotically stable.

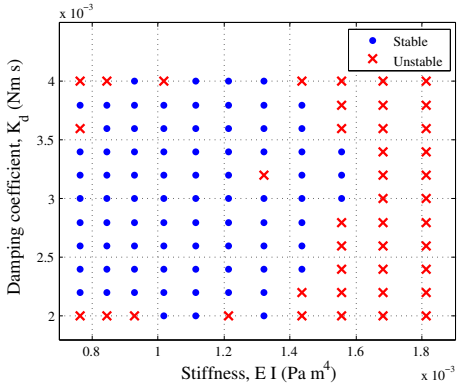

Fig. 13. Stable/Unstable points which there exists a limit cycle and $\mathtt{max}\{\lambda\} < 1$ through whole running frequency (1-7 Hz) are plotted. Stability of the systems depends on stiffness, damping coefficient, and running frequency.

The damping coefficient (K_d = 0.003Nm s) at the joint was selected in such a way that the PRBM can be represented as similar to the actual compliant member as possible by observing its settling time for a given load. Since there may be error in observations, various damping coefficients are tested for guaranteeing stability; dynamics of the system can be affected by the damping coefficient.

As varying stiffness, damping coefficient, asymptotically stable/unstable points which there exists a limit cycle and the magnitude of Floquet multipliers are strictly less than 1 through whole running frequency (1-7 Hz) are plotted in Fig. 13. Most unstable systems show chaotic motion rather than diverging, i.e. $\sup_{t\to\infty}\{|y|\} < \infty$. This means that the behavior of the system is bounded but there is no stable limit set, which everything is unpredictable. For the amphibious locomotion, the system with stiffness and damping coefficient such that it is asymptotically stable through all running frequencies is desirable.

V. Discussions and Future Works

Depending on the gait of the robot, pitch and roll stabilities can vary on the ground. As discussed before, it is assumed that the robot uses the trot gait, in which the roll motion is always stable. In reality, a micro-controller controls the phase of each motor with respect to the phase of the reference motor. However, as the running frequency gets higher, precise position level control which enables a gait pattern becomes difficult to achieve because of limits of control/sensor frequency. For water surface locomotion, it is known that the running frequency is even more important than the gait since the lift force purely depends on it. Thus, a velocity level controller that does not take into account the phase of each motor was implemented. Nevertheless, to hold assumptions in this paper, either a new controller which can control the phase at high speed or an analysis of a design which can be stabilized in spite of the gait that is unstable in the roll direction is needed. Since the former has technical problems currently, the latter can be discussed in a future work. For the pitch motion, the geometry of locomotion makes it unstable so a passive tail is implemented, which prevents it falling back. Compliance at the tail also can help pitch motion stability like the footpad and can be studied using the Poincaré map in the future. In addition, for realization of the compliant footpad, polymers such as TC-8772 which has proper range of strain for given stress can be used. Damping coefficient and spring constant for PRBM will be investigated in future works.

VI. Conclusions

The water runner devised for amphibious locomotion with the same legged mechanisms can use a compliant mechanism on the feet to run at high speed. A passive compliant member attached at the end of each leg is introduced, modeled, and analyzed. Modeling of the ground locomotion can be done with the PRBM which simplifies the dynamics of the compliant member and the ground reaction force modeling which uses geometry and kinematics of the contact point. From the equations of motion, dynamic motions of the angle deflection and the contact angle are obtained. For the water surface locomotion, the reduction of the lift force caused by hydrodynamic pressure is tested as varying running frequencies. As a result, the stiffness of the compliant member can be optimized, which is compatible for both environments.

Within the optimized stiffness of the compliant member, stability of motion is quantified by the Floquet multiplier derived by the Poincaré map. It shows asymptotically stable regime depending on stiffness and damping coefficient.

References

[1] R. Suter *et al.*, "Locomotion on the water surface: Propulsive mechanisms of the fisher spider *Dolomedes Triton*," *J. of Exp. Biology*, vol. 200, pp. 2523–2538, October 1994.

[2] Y. S. Song and M. Sitti, "Surface tension driven biologically inspired water strider robots: Theory and experiments," *IEEE Trans. on Robotics and Automation*, vol. 23, pp. 578–589, June 2007.

[3] J. Bush and D. Hu, "Walking on water: Biolocomotion at the interface," *Annual Rev. of Fluid Mech.*, vol. 38, pp. 339–369, January 2006.

[4] A. Crespi, A. Badertscher, A. Guignard, and A. Ijspeert, "Amphibot 1: an amphibious snake-like robot," *Robotics and Autonomous Systems*, vol. 50, pp. 163–175, March 2005.

[5] S. Guo, T. Fukuda, and K. Asaka, "A new type of fish-like underwater microrobot," *IEEE/ASME Trans. on Mechatronics*, vol. 8, pp. 136–141, March 2003.

[6] D. Hu, B. Chan, and J. Bush, "The hydrodynamics of water strider locomotion," *Nature*, vol. 424, pp. 663–666, August 2003.

[7] S. Floyd and M. Sitti, "Design and development of the lifting and propulsion mechanism for a biologically inspired water runner robot," *IEEE Transactions on Robotics*, vol. 24, no. 3, pp. 698–709, June 2008.

[8] H. S. Park, S. Floyd, and M. Sitti, "Dynamic modeling of a basilisk lizard inspired quadruped robot running on water," in *Proc. of the IEEE/RSJ Int. Conference on Intelligent Robots and Systems*, 2008, pp. 3101–3107.

[9] ——, "Roll and pitch motion analysis of a biologically inspired quadruped water runner robot," *International Journal of Robotics Research - submitted*.

[10] S. Floyd, S. Adilak, R. Rogman, and M. Sitti, "Performance of different foot designs for a water running robot," in *Proc. of International Conference on Robotics and Automation*, 2008, pp. 244–250.

[11] R. M. Alexander, *Principles of Animal Locomotion*. Princeton University Press, 2003.

[12] J. J. Chen *et al.*, "Differential leg function in a sprawled-posture quadrupedal trotter," *Journal of Experimental Biology*, vol. 209, pp. 249–259, 2006.

[13] C. T. Farley, J. Clasheen, and T. A. McMahon, "Running springs: Speed and animal size," *Journal of Experimental Biology*, vol. 185, pp. 71–86, 1993.

[14] A. J. Ijspeert *et al.*, "From swimming to walking with a salamander robot driven by a spinal cord model," *Science*, vol. 315, pp. 1416–1420, March 2007.

[15] L. L. Howell and A. Midha, "Parametric deflection approximations for end-loaded, large-deflection beams in compliant mechanisms," *ASME Journal of Mechanical Design*, vol. 117, no. 1, pp. 156–165, March 1995.

[16] L. L. Howell, A. Midha, and T. W. Norton, "Evaluation of equivalent spring stiffness for use in a pseudo-rigid-body model of large-deflection compliant mechanisms," *ASME Journal of Mechanical Design*, vol. 118, no. 1, pp. 126–131, March 1996.

[17] Y.-Q. Yu *et al.*, "Dynamic modeling of compliant mechanisms based on the pseudo-rigid-body model," *ASME Journal of Mechanical Design*, vol. 127, no. 4, pp. 760–765, July 2005.

[18] L. L. Howell, *Compliant Mechanisms*. Willey, New York, 2001.

[19] [Online]. Available: http://iel.ucdavis.edu/chhtml/toolkit/mechanism

[20] K. G. M. Gerritsen, A. J. Bogert, and B. M. Nigg, "Direct dynamics simulation of the impact phase in heel-toe running," *Journal of Biomechanics*, vol. 28, no. 6, pp. 661–668, 1995.

[21] T. S. Parker and L. O. Chua, *Practical Numerical Algorithms for Chaotic Systems*. Springer-Verlag, 1989.

[22] H. K. Khalil, *Nonlinear Systems*. Prentice Hall, 2002.

[23] P. V. Bayly and L. N. Virgin, "An empirical study of the stability of periodic motion in the forced spring-pendulum," *Mathematical and Physical Sciences*, vol. 443, pp. 391–408, 1993.

[24] D. E. Lathrop and E. J. Kostelich, "Characterization of an experimental strange attractor by periodic orbits," *Phys. Rev. A*, vol. 40, no. 7, pp. 4028–4031, 1989.